

Light-induced photodissociation on the lowest three electronic states of NaH molecule

Otabek Umarov (1,2), András Csehi (1), Péter Badankó (1) Gábor J. Halász (3) and
Ágnes Vibók (1,4)

(1) Department of Theoretical Physics, Doctoral School of Physics, University of Debrecen,
H-4002 Debrecen, PO Box 400, Hungary

(2) Department of Optics and Spectroscopy, Samarkand State University,
140104, University blv. 15, Samarkand, Uzbekistan

(3) Department of Information Technology, University of Debrecen,
H-4002 Debrecen, PO Box 400 Hungary

(4) ELI-ALPS, ELI-HU Non-Profit Ltd,
H-6720 Szeged, Dugonics tér 13, Hungary

Abstract

It has been known that electronic conical intersections in a molecular system can also be created by laser light even in diatomics. The direct consequence of these light-induced degeneracies is the appearance of a strong mixing between the electronic and vibrational motions, which has a strong fingerprint on the ultrafast nuclear dynamics. In the present work, pump and probe numerical simulations have been performed with the NaH molecule involving the first three singlet electronic states ($X^1\Sigma^+(X)$, $A^1\Sigma^+(A)$ and $B^1\Pi(B)$) and several light-induced degeneracies in the numerical description. To demonstrate the impact of the multiple light-induced non-adiabatic effects together with the molecular rotation on the dynamical properties of the molecule, the dissociation probabilities, kinetic energy release spectra (KER) and the angular distributions of the photofragments were calculated by discussing the role of the permanent dipole moment as well.

Key words: non-adiabatic coupling; conical intersection; nuclear dynamics; intense laser field; permanent dipole moment;

I. Introduction

Understanding the behavior of atoms and molecules under the effect of strong electromagnetic fields is an extensively investigated research field. There are a large number of theoretical and experimental works available which have been devoted to discuss numerous new phenomena of light-matter interaction. Although many of these works treat the dynamical problem of diatomics, starting investigations from the simplest hydrogen-like ions or molecules to systems with large number of electrons [1–16]. Nevertheless, several other relevant papers tackle the problem of photodissociation and fragmentation of polyatomics as well [17–36].

Molecular dissociation is usually treated within the Born-Oppenheimer (BO) framework, which relies on the separation of the motions of the electrons and nuclei due to different time scale of their motion. In most cases, this approach works well and provides an acceptable treatment of dynamical processes. But at certain nuclear configurations, in particular, in the close vicinity of degeneracy points or conical intersections (CIs), the energy exchange between electrons and nuclei becomes significant and the BO approximation fails [37]. CIs play an important role in non-adiabatic processes acting as efficient funnels for ultrafast interstate crossings typically on the femtosecond time scale [38–42].

It is known that a molecular system must possess at least two independent nuclear degrees of freedom so as to form a CI. Therefore, having only one nuclear vibrational mode like in the case of diatomics, CIs can never appear. Nevertheless, if an additional degree of freedom like the rotation is associated with the system due to some interactions with the environment (e.g. laser-molecule interaction), CIs can arise. It has been found that, by applying external laser field, light-induced avoided crossings (LIACs) and/or light-induced conical intersections (LICI) can be formed even in diatomics [43]. In contrast to the ACs and CIs occurring in nature, the energy at which the LIACs and LICIs are found, and their non-adiabatic strengths can be controlled by the laser intensity and frequency, respectively. By changing the position and structure of these objects, it is possible to manipulate the non-adiabatic dynamics in molecular systems.

Detailed theoretical and experimental investigations demonstrate that the LICIs can have significant impact on several spectroscopic, dynamical and topological properties of both diatomic [44–55]

and polyatomic [56–58] systems.

As is known the NaH molecule has an astrophysical importance and the photodissociation is one of the channels for the destruction of this alkali hydride molecule in interstellar clouds. In the present paper, we perform pump and probe numerical simulations so as to investigate the non-adiabatic light-induced photodissociation process of the NaH molecule [59–62] in the presence of molecular rotation. The inclusion of the rotation in the dynamical description makes it possible to take appropriately into account the light-induced non-adiabatic effect generated by the strong laser field. Two and one-dimensional numerical simulations are performed, in which, in addition to the molecular vibration the rotation will also be included considering it either as a dynamic variable (2D scheme, LICI framework) or only as a parameter (1D scheme, LIAC framework). Three electronic states ($X^1\Sigma^+(X)$, $A^1\Sigma^+(A)$ and $B^1\Pi(X)$) are involved in the numerical descriptions and particular attention will be paid to the proper discussion of the role of the permanent dipole moment that was completely neglected before [59–62]. In order to exhaustively describe the light-induced non-adiabatic dissociation dynamics of this system, several different dynamical properties like dissociation probabilities, kinetic energy release spectra (KER), as well as fragment angular distributions have been studied.

The article is structured as follows. In the next section, the methodology and algorithms required for the theoretical study are presented. Namely, the working Hamiltonian, the applied electric fields, the calculated dynamical quantities as well as the numerical details are briefly summarized. In the third section, we present and discuss the numerical results for the NaH system. Finally, in the last part, conclusions will be given.

II. Methodology and physical background

In what follows, a brief summary will be provided concerning the electronic structure quantities of NaH. Then the time-dependent nuclear Hamiltonian, which governs the dynamics of the system will be defined. In the last two parts of this section a brief description of the time-dependent electric field of the applied laser pulses, the theoretical approach used to compute the time evolution of the

nuclear wave packet, as well as the expressions of the computed dynamical quantities are given.

A. The sodium hydride molecule

In our numerical simulations, the NaH molecule is described as a three-level system involving the three lowest-lying singlet electronic states, namely $X^1\Sigma^+(X)$, $A^1\Sigma^+(A)$ and $B^1\Pi(B)$ (labeled throughout the paper as $V_X(R)$, $V_A(R)$ and $V_B(R)$). The corresponding potential energy curves are visualized in Fig. 1a. Figures 1b and 1c present the transition ($\vec{\mu}_{i,j}(R) = \langle \phi_i | \Sigma_k \vec{r}_k | \phi_j \rangle$) and the permanent ($\vec{\mu}_i(R) = \langle \phi_i | \Sigma_k \vec{r}_k | \phi_i \rangle$) dipole moments (TDM and PDM) ($i, j \in (X, A, B)$), respectively. It should be noted that all the permanent dipole moments and the transition dipole moment $\vec{\mu}_{X,A}$ are parallel with the molecular axis, while the ones corresponding to the $\Sigma - \Pi$ transition ($\vec{\mu}_{X,B}$ and $\vec{\mu}_{A,B}$) are perpendicular. Numerical computation of these electronic structure quantities has been carried out by using the MOLPRO program package [63] at the MRCI/CAS(2/9)/aug-cc-pV5Z level of theory. The number of active electrons and MOs in the individual irreducible representations of the C_{2v} point group were $A \rightarrow 2/5, B_1 \rightarrow 0/2, B_2 \rightarrow 0/2, A_2 \rightarrow 0/0$. By using these values we could achieve reasonable agreement with other results in the literature [64, 65].

B. The working Hamiltonian

In the space of the three lowest singlet electronic states the following full time-dependent nuclear Hamiltonian of NaH holds for the rovibronic nuclear motions:

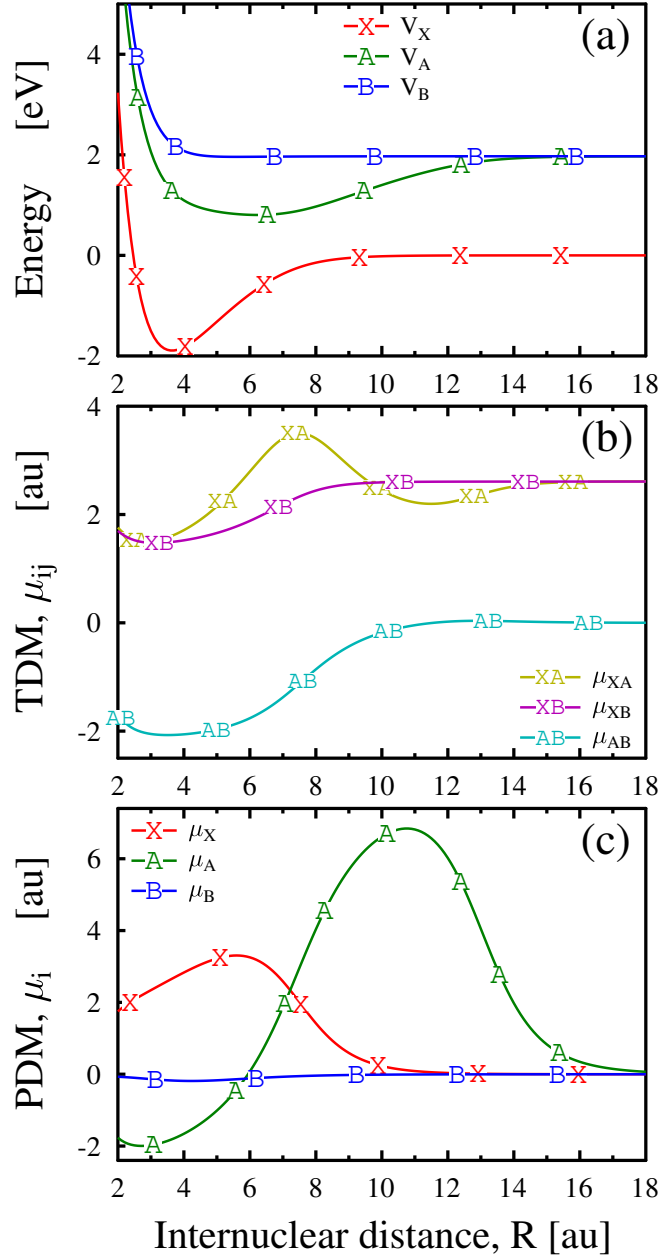


Figure 1: (a) Lowest three adiabatic potential energy curves of the NaH molecule. (b) Transition dipole moment (TDM) functions between the different adiabatic electronic states. (c) Permanent dipole moment (PDM) functions of the three adiabatic electronic states.

$$\begin{aligned}
H = & \left(-\frac{1}{2M_r} \frac{\partial^2}{\partial R^2} + \frac{L_\theta^2}{2M_r R^2} \right) \cdot \mathbf{1} + \begin{pmatrix} V_X(R) & 0 & 0 \\ 0 & V_A(R) & 0 \\ 0 & 0 & V_B(R) \end{pmatrix} + \\
& -E(t) \begin{pmatrix} \mu_X \cos(\theta) & \mu_{X,A} \cos(\theta) & \mu_{X,B} \sin(\theta) \\ \mu_{A,X} \cos(\theta) & \mu_A \cos(\theta) & \mu_{A,B} \sin(\theta) \\ \mu_{B,X} \sin(\theta) & \mu_{B,A} \sin(\theta) & \mu_B \cos(\theta) \end{pmatrix}.
\end{aligned} \tag{1}$$

Here the first term in H describes the kinetic energy of the system with R and θ being the molecular vibrational and rotational coordinates, respectively. $\mathbf{1}$ is the three-dimensional unit matrix, M_r is the reduced mass, and L_θ is the angular momentum operator of the nuclei with $m = 0$. The rotational coordinate θ , represents the angle between the internuclear axis and the laser polarization direction. $V_X(R)$, $V_A(R)$ and $V_B(R)$ are the first three singlet electronic states. The third term represents the light-matter interaction in dipole approximation. $E(t)$ characterizes the time-dependent electric field and the dipole matrix contains the permanent as well as the transition dipole moments, as these were defined in the former section. Atomic units ($e = m_e = \hbar = 1$) are used throughout the article. Expression given by Eq. (1) will be used throughout the paper, as the working Hamiltonian.

C. The applied electric field

The linearly polarized $E(t)$ laser field applied in the simulations is the sum of two components:

$$E(t) = E_{pm} f_{pm}(t) \cos(\omega_{pm} t) + E_{pr} f_{pr}(t) \cos(\omega_{pr} t). \tag{2}$$

The first term represents a pump pulse with energy $\hbar\omega_{pm}$ and amplitude E_{pm} which initiates the dynamics of the system by transferring some amounts of the initial ground $V_X(R)$ state population to the excited $V_A(R)$ state. The second term provides a probe pulse with energy $\hbar\omega_{pr}$ and amplitude E_{pr} transferring further the population from the $V_A(R)$ state to the other two $V_X(R)$ and $V_B(R)$ dissociation channels. Cos-square-shaped pulses were used for the envelope functions of the pump

$f_{\text{pm}}(t)$ and probe $f_{\text{pr}}(t)$ pulses:

$$f_{\text{pm}}(t) = \cos^2 \left(\frac{\pi(t - t_{\text{pm}})}{\tau_{\text{pm}}} \right) \quad (3)$$

$$f_{\text{pr}}(t) = \cos^2 \left(\frac{\pi(t - t_{\text{pr}})}{\tau_{\text{pr}}} \right). \quad (4)$$

Here $t_{\text{pm}} = 0$ fs and $t_{\text{pr}} = 0 \dots 1000$ fs are the centers, while τ_{pm} and τ_{pr} are the durations of the pump and probe laser pulses, respectively. One can define the delay time as: $t_{\text{del}} = t_{\text{pr}} - t_{\text{pm}}$. During the numerical simulations the energy, the intensity and the duration of the pump and probe pulses were fixed. For the pump pulse an efficient population was provided by the parameters $\omega_{\text{pm}} = 3.24$ eV, $I_{\text{pm}} = 1 \cdot 10^{13}$ W/cm² and $\tau_{\text{pm}} = 8$ fs, while for the probe pulse the $\omega_{\text{pr}} = 1.08$ eV, $I_{\text{pr}} = 1 \cdot 10^{12}$ W/cm² and $\tau_{\text{pr}} = 20$ fs parameters were able to couple properly the $V_{\text{A}}(\text{R})$ state with the $V_{\text{X}}(\text{R})$ and $V_{\text{B}}(\text{R})$ channels.

So as to demonstrate the essence of the LICI phenomenon we can borrow the Floquet framework of the nuclear Hamiltonian (see [44–47] for a detailed discussion). This presentation provides an illustrative picture and is frequently used to understand different phenomena in the field of light-matter physics (see in Fig. 2).

In this picture, the pump laser pulse shifts the energy of the $V_{\text{X}}(\text{R})$ ground potential curve by $\hbar\omega_{\text{pm}}$ and a crossing ($\text{LICI}_{\text{pump}}$) between the shifted ground ($V_{\text{X}}(\text{R}) + \hbar\omega_{\text{pm}}$) and the first excited potential energy $V_{\text{A}}(\text{R})$ curves is created (see Fig. 2a). This process then initiates a wave packet dynamics on the state $V_{\text{A}}(\text{R})$ which can be tested by a probe laser pulse which couples the $V_{\text{A}}(\text{R})$ both to the $V_{\text{B}}(\text{R})$ as well as to the $V_{\text{X}}(\text{R})$ potential energy states. The action of the probe pulse can be described in the Floquet framework, as the $V_{\text{A}}(\text{R})$ first excited potential curve being shifted upwards and downwards by $\hbar\omega_{\text{pr}}$. Crossings between the upwards shifted first excited ($V_{\text{A}}(\text{R}) + \hbar\omega_{\text{pr}}$) and the second excited $V_{\text{B}}(\text{R})$ potential energy curves, as well as the downwards shifted first excited ($V_{\text{A}}(\text{R}) - \hbar\omega_{\text{pr}}$) and the ground $V_{\text{X}}(\text{R})$ potential energy curves are created, respectively. We note that the pump pulse has already created a $\text{LICI}_{\text{pump}}$ between the shifted ground ($V_{\text{X}}(\text{R}) + \hbar\omega_{\text{pm}}$) and the first excited $V_{\text{A}}(\text{R})$ potential energy curves (see Fig. 2a), and its effect is manifested in the initiation

of the wave packet rotation dynamics on the $V_A(R)$. By diagonalizing the corresponding Floquet form of the working Hamiltonian Eq.(1), one can obtain the light-induced adiabatic potential energy surfaces which can be seen in Fig. 2b. The corresponding light-induced adiabatic surfaces cross each other giving rise to light-induced conical intersections whenever the conditions $\sin \vartheta = 0$ ($\vartheta = 0, \vartheta = \pi$) and $(V_A(R) - \hbar\omega_{pr}) = V_X(r)$ as well as $\cos \vartheta = 0$ ($\vartheta = \pi/2$) and $(V_A(R) + \hbar\omega_{pr}) = V_B(r)$ are simultaneously fulfilled. For the parallel transition, the $\sin \vartheta$ factors are replaced by $\cos \vartheta$ in Eq.(1). Namely, for perpendicular transitions, the LICIs occur at $\vartheta = 0; \vartheta = \pi$, while for parallel transitions, at $\vartheta = \pi/2$. For those laser parameters which are applied during the present calculations two LICIs (LICI1 and LICI2) and one LIAC are formed by the effect of the probe pulse (see Fig. 2a).

It is important to emphasize that in contrast to the case provided by natural CIs of field-free molecules, the LICI is controllable in the sense that the laser frequency determines its position and energy in the nuclear configuration space, while the strength of the coupling is given by the laser intensity.

D. Nuclear wave packet propagation and calculated quantities

The non-adiabatic nuclear dynamics is governed by the Hamiltonian in Eq. (1) which contains the vibrational and rotational degrees of freedom of the molecule. To study the photodissociation in the LICI framework, one has to solve the time-dependent Schrödinger equation (TDSE) by applying this Hamiltonian. One of the most efficient approaches for this is the MCTDH (multiconfigurational time-dependent Hartree) method [66–68]. The vibrational degree of freedom (R) was characterized by using FFT-DVR (Fast Fourier Transformation-Discrete Variable Representation) with $N_R = 512$ grid points distributed within the range from 2.0 au to 50 au for the internuclear separation. The rotational degree of freedom was described by Legendre polynomials $\{P_J(\cos \theta)\}_{j=0,1,2,\dots,N_\theta}$. These so called primitive basis sets (χ) were used to represent the single particle functions (ϕ), which in turn

were applied to represent the wave function:

$$\begin{aligned}\phi_{j_q}^{(q)}(q, t) &= \sum_{l=1}^{N_q} c_{jql}^{(q)}(t) \chi_l^{(q)}(q) \quad q = R, \theta \\ \psi(R, \theta, t) &= \sum_{j_R=1}^{n_R} \sum_{j_\theta=1}^{n_\theta} A_{j_R, j_\theta}(t) \phi_{j_R}^{(R)}(R, t) \phi_{j_\theta}^{(\theta)}(\theta, t).\end{aligned}\tag{5}$$

In the actual calculations, we have used $N_\theta = 91$ and for both degrees of freedom a set of $n_R = n_\theta = 28$ single particle functions were applied to construct the nuclear wave packet. In all simulations, the convergence was tested with these parameters.

The solution of the nuclear TDSE with the ansatz in equation 5 is utilized to calculate the kinetic energy release (KER) $P_{\text{KER}}(E)$, the total dissociation probability P_{diss} and the angular distribution $P(\theta_j)$ of the dissociation fragments. The kinetic energy release (KER) of the photofragments is [68]:

$$P_{\text{KER}}(E) = \int_0^\infty dt \int_0^\infty dt' \langle \psi(t) | W | \psi(t') \rangle e^{-iE(t-t')} \tag{6}$$

where $-iW$ is the complex absorbing potential (CAP) applied at the last 10 au of the grid related to the vibrational degree of freedoms ($W = 0.000012 \cdot (R - 40)^3$, if $R > 40$ au on all three surfaces) and

$$P(\theta_j) = \frac{1}{w_j} \int_0^\infty dt \langle \psi(t) | W_{\theta_j} | \psi(t) \rangle \tag{7}$$

where $-iW_{\theta_j}$ is the projection of the CAP to a specific point of the angular grid ($j = 0, \dots, N_\theta$), and w_j is the weight related to this grid point according to the applied DVR.

The total dissociation probability can be determined as [68]:

$$P_{\text{diss}} = \int_0^\infty dE \cdot P_{\text{KER}}(E). \tag{8}$$

Throughout the calculations, the initial nuclear wave function (at $t \ll t_{\text{pm}}$) was assumed to be in its vibrational and rotational ground state ($\nu = 0$; $J = 0$). Initially, the molecules are assumed in the numerical calculations to be nonaligned and isotropically distributed and subject to linearly polarized \cos^2 pump and probe laser pulses centered around $t_{\text{pm}} = 0$ fs and $t_{\text{pr}} = 0 - 1000$ fs, respectively.

To demonstrate the impact of light-induced non-adiabatic effect on the dissociation dynamics of the NaH, results obtained from the full two-dimensional (2D) and one-dimensional (1D) models were compared. In the 2D case both the rotational and vibrational coordinates are accounted for as dynamical variables while in the 1D situation, the rotational degree of freedom (θ) is used only as a parameter and accordingly, only LIACs and not LICI can be considered. In the 1D model the molecule's initial orientation is not changing during the dynamics and the “effective field strength” was the projection of the real field on the direction of the actual dipole moment. Both the transition dipole between the $V_X(R)$ and $V_A(R)$ energy states and all the permanent dipoles are parallel to the axis of the molecule, so $\varepsilon_0^{\text{eff}}(\theta) = \varepsilon_0 \cos \theta$ (i.e., with an effective intensity of $I_0^{\text{eff}}(\theta) = I_0 \cos^2 \theta$). For the transition dipoles related to a $\Sigma \longleftrightarrow \Pi$ electronic transition (μ_{XB} and μ_{AB}) the dipoles are perpendicular to the molecular axis, therefore $\varepsilon_0^{\text{eff}}(\theta) = \varepsilon_0 \sin \theta$ (i.e., with an effective intensity of $I_0^{\text{eff}}(\theta) = I_0 \sin^2 \theta$).

III. Results and discussion

In this section, we investigate the non-adiabatic dissociation dynamics of a molecular system. As mentioned in the introduction our aim is to perform a pump and probe numerical simulation for the NaH molecule, so as to demonstrate the impact of the light-induced non-adiabatic phenomena on the dissociation dynamics. To study this effect the three lowest-lying singlet electronic states and an initial isotropic distribution of the molecular ensemble are considered. The corresponding transition dipole matrix elements are responsible for the light-induced electronic transitions.

In Figure 2 the corresponding potential energy surfaces and the light-dressed states are visualized. At first, by using a pump pulse a part of the ground $V_X(R)$ electronic state population is transferred to the first excited $V_A(R)$ state. Then with a time delay the probe pulse couples the $V_A(R)$ state to the $V_X(R)$ and $V_B(R)$ ones by transferring further a reasonable amount of the $V_A(R)$ population to these states. With the pump pulse applied, more than 50% of the ground state population is transferred from the $V_X(R)$ state to the $V_A(R)$ one. The dynamics therefore is initiated on the $V_A(R)$ state, but the essential part of the dissociation occurs on the $V_X(R)$ and $V_B(R)$ states. The

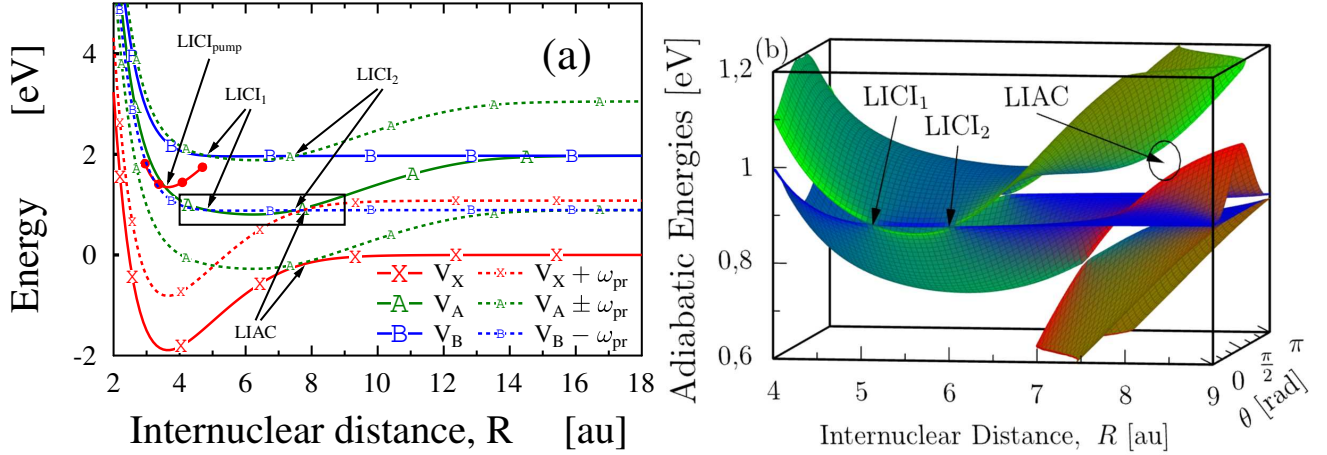


Figure 2: (a) The three lowest-lying singlet adiabatic potential energy curves of the NaH molecule. The corresponding light-dressed states are denoted by dashed lines. The position of the light-induced conical intersections (LICI_{pump}, LICI1 and LICI2) and avoided crossing (LIAC) are also marked. (b) Light-induced potential energy surfaces for the three-state model calculated for the field intensity $I_{pr} = 1 \cdot 10^{12} \text{ W/cm}^2$. The coloring reflects the diabatic states that make up the different points of the adiabatic surfaces: red, $V_X(R)$; green, $V_A(R)$; and blue, $V_B(R)$.

$V_B(R)$ is already a dissociative state, but dissociation can also occur on $V_X(R)$ due to the fact that the population arrives here with sufficiently large kinetic energy.

Figure 3 shows the field-free time evolution of the nuclear wave packet on the $V_A(R)$ potential energy surface after using a pump pulse. The field-free wave packet oscillates back and forth on the interval of $R \approx 3 - 11$ au. Initially and in the first quarter of the studied time domain it is relatively well localized, while in the last quarter it is rather diffuse. Although it is still possible to recognize its periodicity in this latter time domain, but it can no longer be localized with a relatively good approximation. The dashed lines (at $R = 4.85$ au and $R = 7.5$ au) are the positions of the LICI1 and LICI2 between the $V_A(R)$ and $V_B(R)$ surfaces, while the dotted line (at $R = 7.8$ au) is the position of the LIAC between the $V_A(R)$ and $V_X(R)$. It is expected that the dissociation yields on the corresponding surfaces will be large for those values of the t_{del} where these horizontal lines intersect with the nuclear wave packet (at the position of LICI1, LICI2 and LIAC). Namely, at $t \approx 15, 90, 110 \dots \text{fs}$ on the $V_B(R)$ state and at $t \approx 30, 70, \dots \text{fs}$ on the $V_X(R)$ state. We note here that due to the large transition dipole moment values (see Fig. 1b), the influence of LICI1 and LIAC on the non-adiabatic dynamics is more significant than that of the LICI2.

In Fig. 4 the dissociation probabilities correspond to each of the individual states, as well as

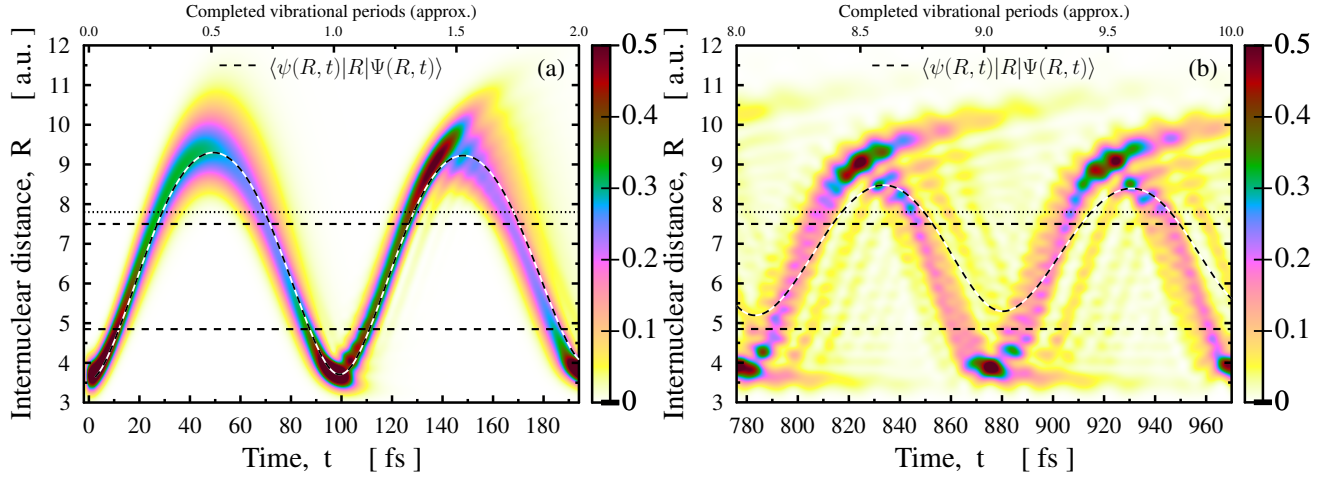


Figure 3: Field-free vibrational motion of the nuclear wave packet – after applying the pump pulse – on the $V_A(R)$ potential energy curve. The time dependent density of the nuclear wave packet is displayed in an initial ($t \approx 0 - 190$ fs) and a final ($t \approx 750 - 980$ fs) time periods by color map. The darker the color, the larger the value of the nuclear density. In addition, the time-dependent average of the internuclear distance (dashed line) is also shown. The dashed lines (at $R = 4.85$ au and $R = 7.5$ au) are the positions of the LIC1 and LIC2 between $V_A(R)$ and $V_B(R)$, while the dotted line (at $R = 7.8$ au) is the position of the LIAC between $V_A(R)$ and $V_X(R)$.

the sum of them as a function of time delay (t_{del}) are displayed. At first glance, it is obvious that a significant part of the dissociation takes place from surface $V_B(R)$. The dissociation probability of the $V_X(R)$ state at certain time delays can be up to 10-12%, while in the case of $V_B(R)$ it can even go over 40% of the whole population. The dissociated population of the $V_X(R)$ state originates from the population of the initially populated $V_A(R)$ state. For the case of the $V_B(R)$ state the 2% of the dissociated population originates from the effect of the pump pulse, and the remaining large amount of the dissociated population arises due to the population transfer of the $V_A(R)$ state by the probe pulse, as for the case of the $V_X(R)$. From the third state $V_A(R)$, the dissociation yield is about two orders of magnitude smaller and therefore it is practically invisible on the scale used. Consequently, the period of the total dissociation yield is practically dominated by the period of the dissociation yield occurring on the $V_B(R)$. One can also notice that the structure of the dissociation yields obtained from the $V_X(R)$ and $V_B(R)$ states, as well as the curve of the total yield are different. The origin of the difference can easily be understood based on Fig. 3. The dissociation yields possess large values at those t_{del} delay times where the field-free wave packet has a significant amplitude in the close vicinity of the LICs and LIAC positions. These points are the intersection

points of the wave packet and the horizontal lines in Fig. 3. The intersection points – between the position of LIC1 and the wave packet – are closer to the turning point of the nuclear vibration, therefore the peaks on the yield curve from the $V_B(R)$ state are also closer to each other than that of the $V_X(R)$ state. The two panels of Fig. 4 compare the results of the 1D and 2D calculations. It can be seen that the amplitude of the dissociation yields decrease monotonically as a function of time delay, and this decreasing is more prominent in the 2D results. Although the magnitude of the amplitudes decreases, their minimum values continuously increase, while their maximum values continuously decrease as a function of time delay. This effect is due to the increasing blurring of the nuclear wave packet at increasing t_{del} values. The differences between the 1D and 2D results can be interpreted, as a fingerprint of the molecular rotation combined with the effects of the LICs and LIAC as well as with the different magnitudes/directions of the respective transition dipole moments. The pump pulse transfers a part of the population to surface $V_A(R)$, and at the same time initiates the rotation of the wave packet. After the pump process, as time increases, the molecular axis rotates closer and closer to the polarization direction of the pump pulse. On the one hand, when the probe appears, it transfers further a part of the population from $V_A(R)$ to $V_B(R)$. Because the transition dipole moment between these two states is perpendicular to the molecular axis, it can transfer less population than in the case of 1D, when the rotation is frozen. On the other hand, the probe can also couple the $V_A(R)$ and $V_X(R)$ states and it provides more efficient population transfer due to the parallel direction of the $\mu_{A,X}$ to the polarization direction of the probe pulse. Consequently, it starts to transfer back some parts of the population to the $V_A(R)$ state and Rabi oscillation starts between these two states. Finally, it slightly suppresses the total dissociation yield relative to the 1D model.

To clearly visualize the dependence of the kinetic energy release (KER) of the photofragments as a function of time delay, results for the three individual states are displayed in Fig. 5. For the case of shorter delay times the 1D and 2D results are quite the same, therefore only the 1D spectra are presented. The fact that the two different models are almost identical for these short delay times means that the rotation initialized by the pump pulse on surface $V_A(R)$ has not yet been significantly developed before the probe pulse hits the system. Contrary to this, for larger delay times, the difference between the two descriptions is already noticeable. Here, in the photofragment

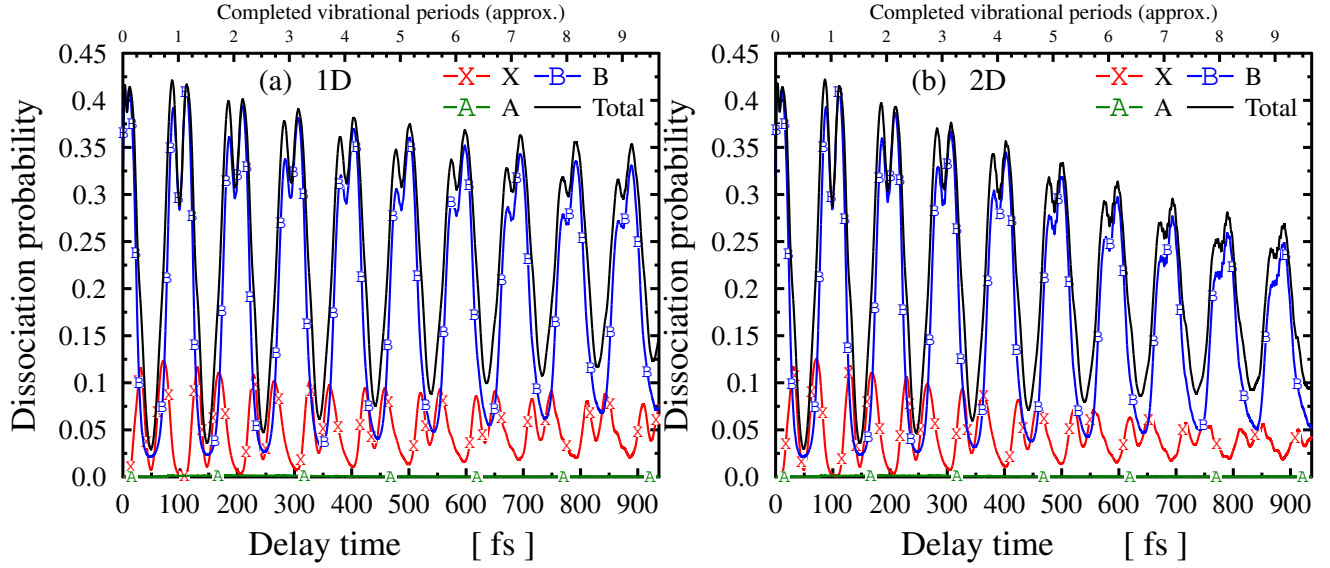


Figure 4: Dissociation probabilities corresponding to each of the individual adiabatic electronic states as well as the sum of them as a function of time delay between the pump and probe pulses. Calculations are displayed both in the 1D and 2D models (see on panel (a) and (b), respectively).

KER spectra of the different states, one can clearly recognize the three-dimensional fingerprint of the dissociation yields obtained from the corresponding channels. Namely, the 1D model always provides a more significant dissociation yield on the $V_X(R)$ and $V_B(R)$ states than that of the 2D one.

To further analyze the dissociation process, the fragment angular distributions of the $V_X(R)$ ground electronic state are displayed in Fig. 6. In panel (a) the 1D results are presented for short delay times. In this case, the molecules do not rotate and because the transition dipole moment is parallel to the molecular axis between the $V_X(R)$ and $V_A(R)$ states, nothing appears at around $\theta = 90$ degrees. The pump pulse does not only transfer the population to the $V_A(R)$, but also takes it back to $V_X(R)$. Similarly, the probe does not only transfer from the $V_A(R)$ to $V_X(R)$, but also takes it back to $V_A(R)$. Due to the larger coupling at around $\theta = 0$ degree, two-photon process is also present. The periodic change of the maximum values is consistent with the movement of the nuclear wave packet (see Fig. 3). At larger delay times the fragment angular distribution is much more spread out which is related to the diffuse character of the nuclear wave packet (see Fig. 3b). However, the maximum values remained at the same position as in the short t_{del} . Since the molecules cannot rotate, the positions of the maximum values depend on what kind of molecular distribution has been developed right immediately after the effect of the pump pulse. In Fig. 6c results of the 2D simulations are

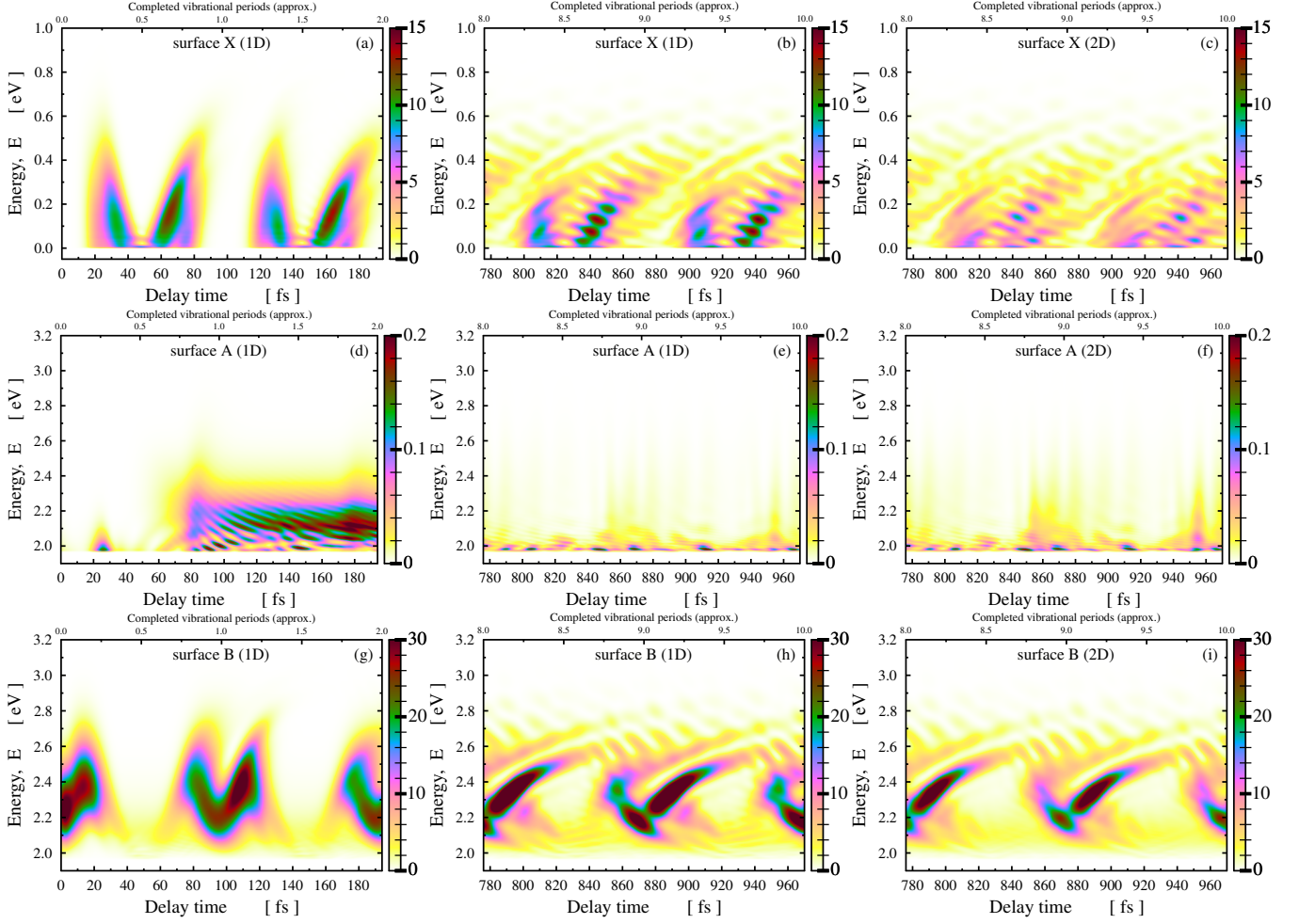


Figure 5: Kinetic energy release spectra (KER) of the photofragment of the NaH molecule as a function of delay time. Results are presented for each of the individual channels in the 1D as well as in the 2D framework.

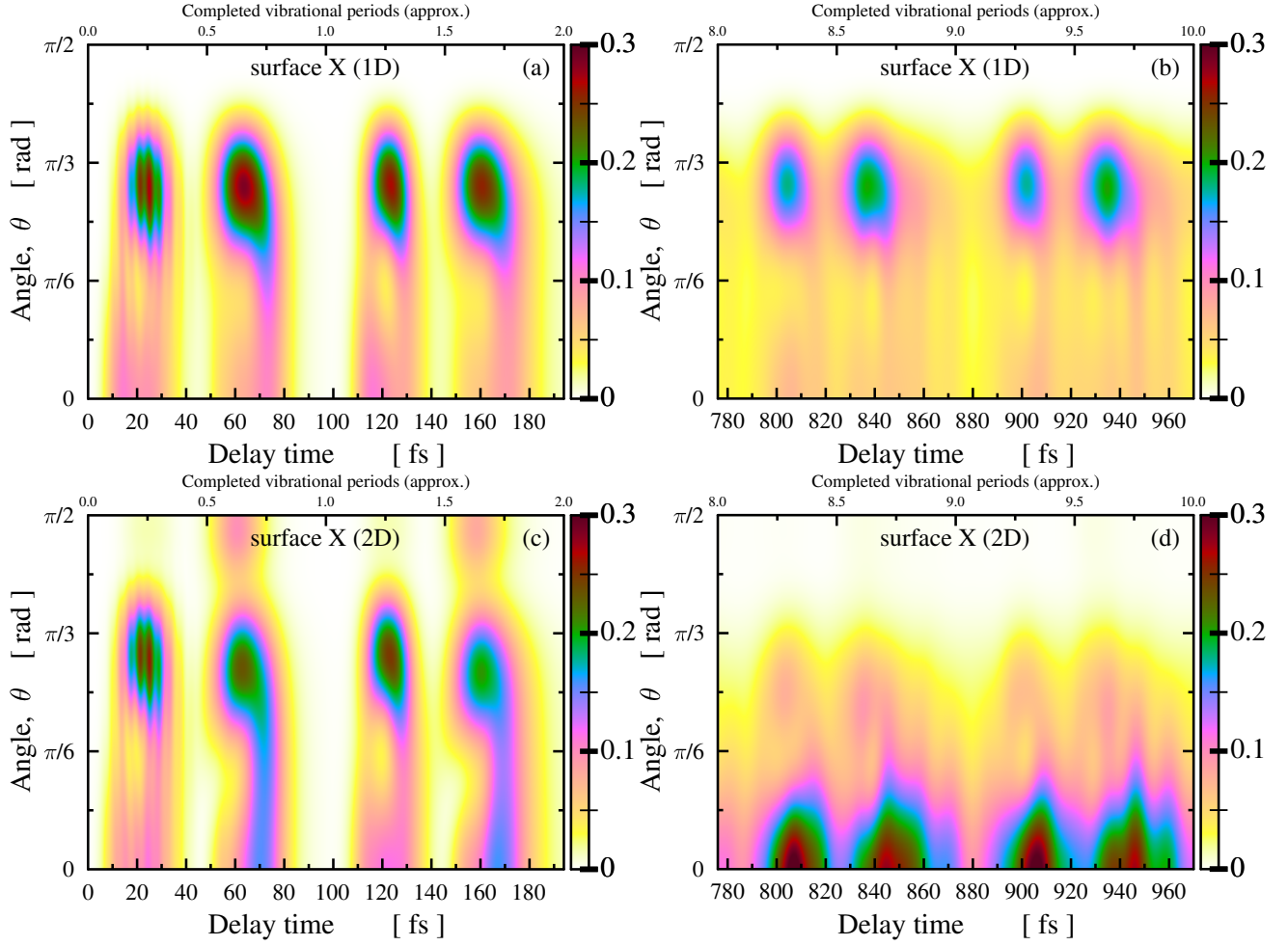


Figure 6: Fragment angular distribution of the dissociating NaH molecule for the $V_X(R)$ electronic state as a function of time delay. Results are presented both for the 1D and 2D schemes.

presented for short delay times. The maximum values of the 2D angular distributions are at the same position as for the 1D case, but the effect of the rotation appears, as well. Consequently, enhanced 2D dissociation occurs at certain time delays ($t_{\text{del}} = 60$ fs and $t_{\text{del}} = 160$ fs) at $\theta = 0$ degree. Within this time interval, the difference between the 1D and 2D schemes is not really significant, except for that at $t_{\text{del}} = 60$ fs and $t_{\text{del}} = 160$ fs time delays dissociation can take place at around $\theta = 90$ degree. The latter can be explained by the fact that the probe pulse rotates the molecule to the direction of $\theta = 0$ degree on the lower and to the direction of $\theta = 90$ degrees on the upper adiabatic surfaces. Depending on in which state it was for longer times, rotates towards $\theta = 0$ or $\theta = 90$ degrees during the dissociation. In contrast, at longer delay times the situation is completely different (see Fig. 6d). Here, because of the effect of the pump pulse the system has already had enough time to rotate towards the polarization direction of the pump pulse and consequently, the largest dissociation yield can be obtained at around $\theta = 0$ degree. The periodic structure is also visible here, but it is much more blurred than at shorter delay times (see Fig. 6c).

It can be seen in Fig. 7 that the amount of the dissociation yield of the $V_A(R)$ state is almost negligible. Both in the 1D and 2D schemes this amount is two orders of magnitude smaller than that of the two other states. Nevertheless, it is still worth analyzing the structure of these panels. Again, at short delay times the 1D and 2D results are similar. Only very small differences can be realized in very small quantities. On the contrary, at large delay times at around $t_{\text{del}} = 850$ fs an interesting phenomenon is experienced. The dissociation yield increases on the $V_A(R)$ state in the 2D model. The reasons might be as follows: i) the pump pulse does not only transfer the populations but also rotates the molecules and at a long delay time - before the probe pulse is switched on - the molecules could rotate close to the polarization direction of the pump pulse; ii) because two-photon process might be initiated, the probe pulse can also transfer back some populations from the $V_X(R)$ and $V_B(R)$ states to the $V_A(R)$. By collecting sufficiently large kinetic energy due to the rovibration, the dissociation yield from the $V_A(R)$ surface can increase. In this process, due to the direction of the $\mu_{X,A}$, the population transfer from the $V_X(R)$ state via the LIAC has a more significant importance. The fingerprint of the latter effect can clearly be seen in Fig. 9b as well, which will be further discussed.

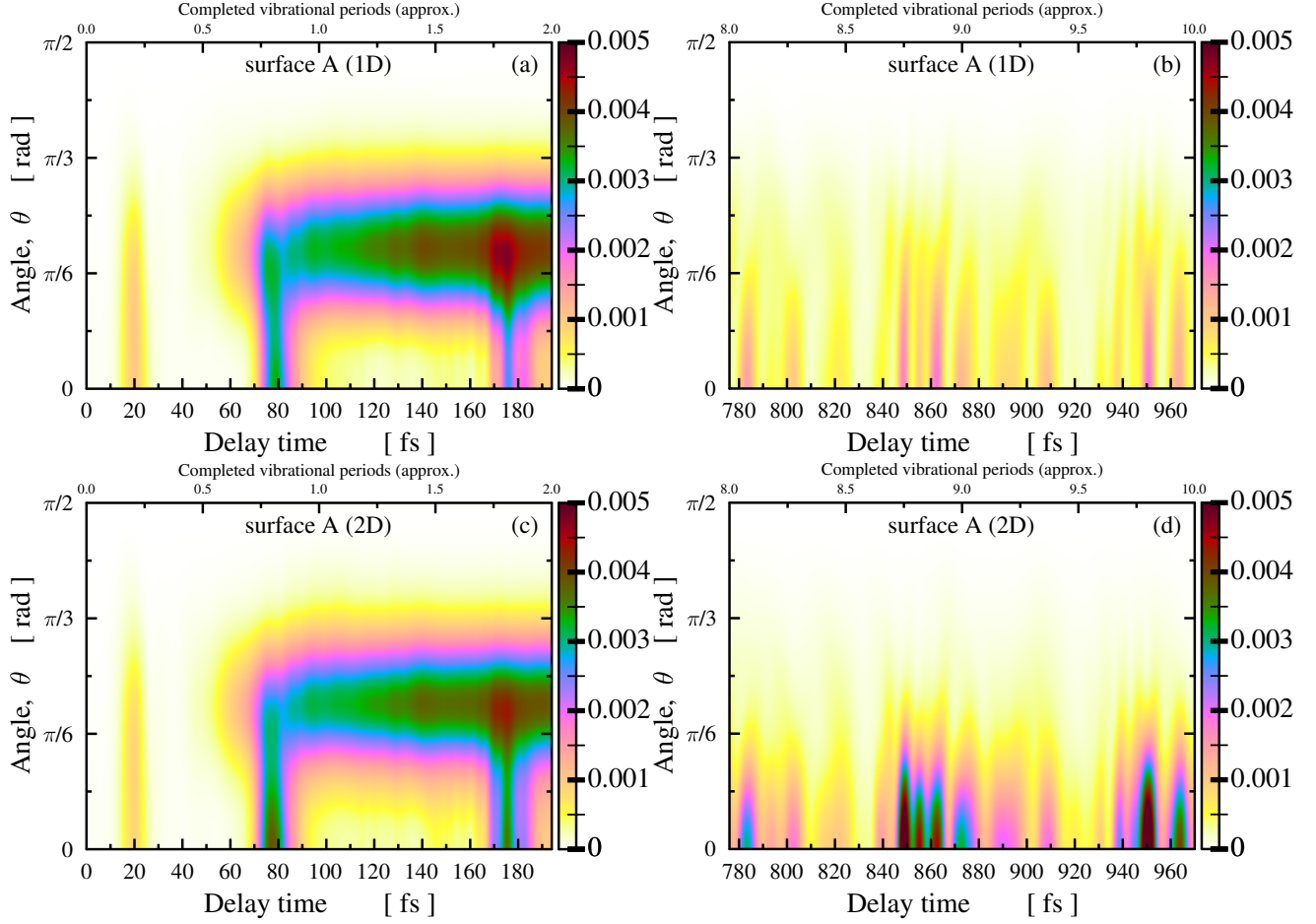


Figure 7: Fragment angular distribution of the dissociating NaH molecule for the $V_A(R)$ electronic state as a function of time delay. Results are presented both for the 1D and 2D schemes.

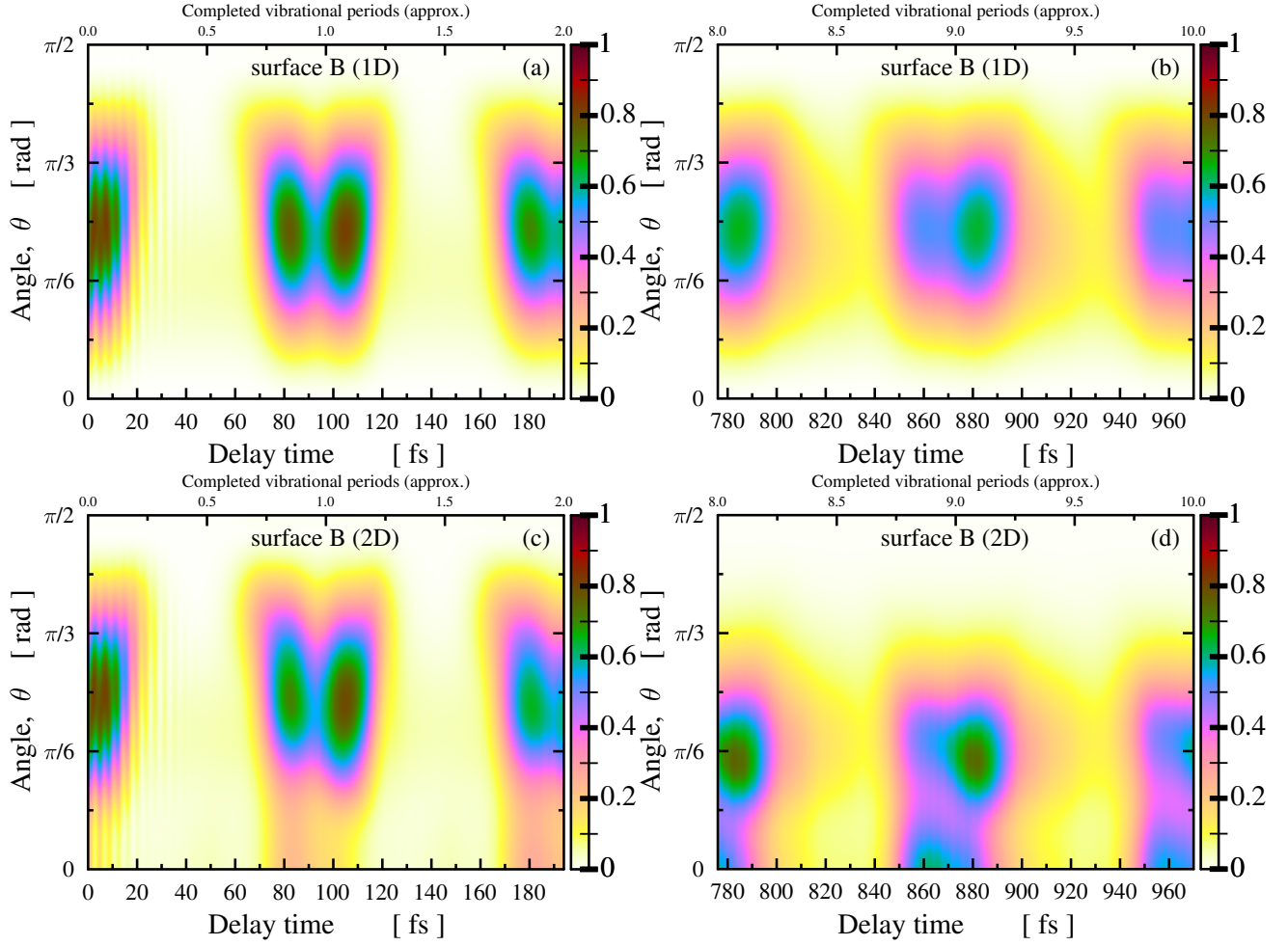


Figure 8: Fragment angular distribution of the dissociating NaH molecule for the $V_B(R)$ electronic state as a function of time delay. Results are presented both for the 1D and 2D schemes.

Fragment angular distribution of the $V_B(R)$ state is displayed in Fig. 8. In the 1D scheme it is immediately apparent that dissociation does not occur either at $\theta = 0$ or at $\theta = 90$ degrees. At $\theta = 90$ degrees the pump pulse does not transfer molecules to the $V_A(R)$ state in this direction. While at $\theta = 0$ the reason for the lack of dissociation yield is that the probe pulse could not transfer further the population from the $V_A(R)$ to $V_B(R)$ as the μ_{AB} is perpendicular to the molecular axis. This tendency holds for the whole studied delay times, because the rotation of the molecules is frozen. In short delay times the essential difference between the 1D and 2D models is that the dissociation appears in 2D even at $\theta = 0$ degree. This effect can then become stronger, as the delay time increases. The pump pulse does not only create an anisotropic angular distribution of population on the $V_A(R)$ state, but also initiates a rotation which further increases this asymmetry, as the delay time goes on. Then the probe pulse comes and with the transition dipole moment μ_{AB} which is perpendicular to the molecular axis can further transfer the population to the $V_B(R)$ state. The transferred molecules continue to rotate further on the $V_B(R)$ state during the dissociation and finally are aligned parallel to the polarization direction. However, this process cannot take place in the 1D model. As the delay time increases, and the rotation becomes more and more significant, the probe pulse finds molecules closer and closer to the polarization direction, therefore the larger values of the fragment angular distribution shift towards to smaller θ angles. Similarly to Figs. 6-7 discussed before, the temporal periodicity of the fragment angular distribution can again be interpreted as the consequence of the behavior of the field-free nuclear wave packet (see Figure 3).

Finally we discuss the role of the permanent dipole moment by means of the investigation of the dissociation yield and the fragment angular distribution from the $V_A(R)$ state. In Fig. 9 the dissociation yields are presented with and without the permanent dipole moment for each of the individual states both in the 1D and 2D schemes. It can be seen in Fig. 9a that independently from the model used - on the applied scale - practically there is no difference between the results obtained with and without using PDM for the case of the $V_X(R)$ state. This finding however, does not completely hold for the $V_B(R)$ state (see on panel (b)) in which minor differences can be realized between the two different results, especially at longer delay times both in the 1D and 2D schemes. However, inspecting Fig. 9c, an interesting observation can be made concerning the

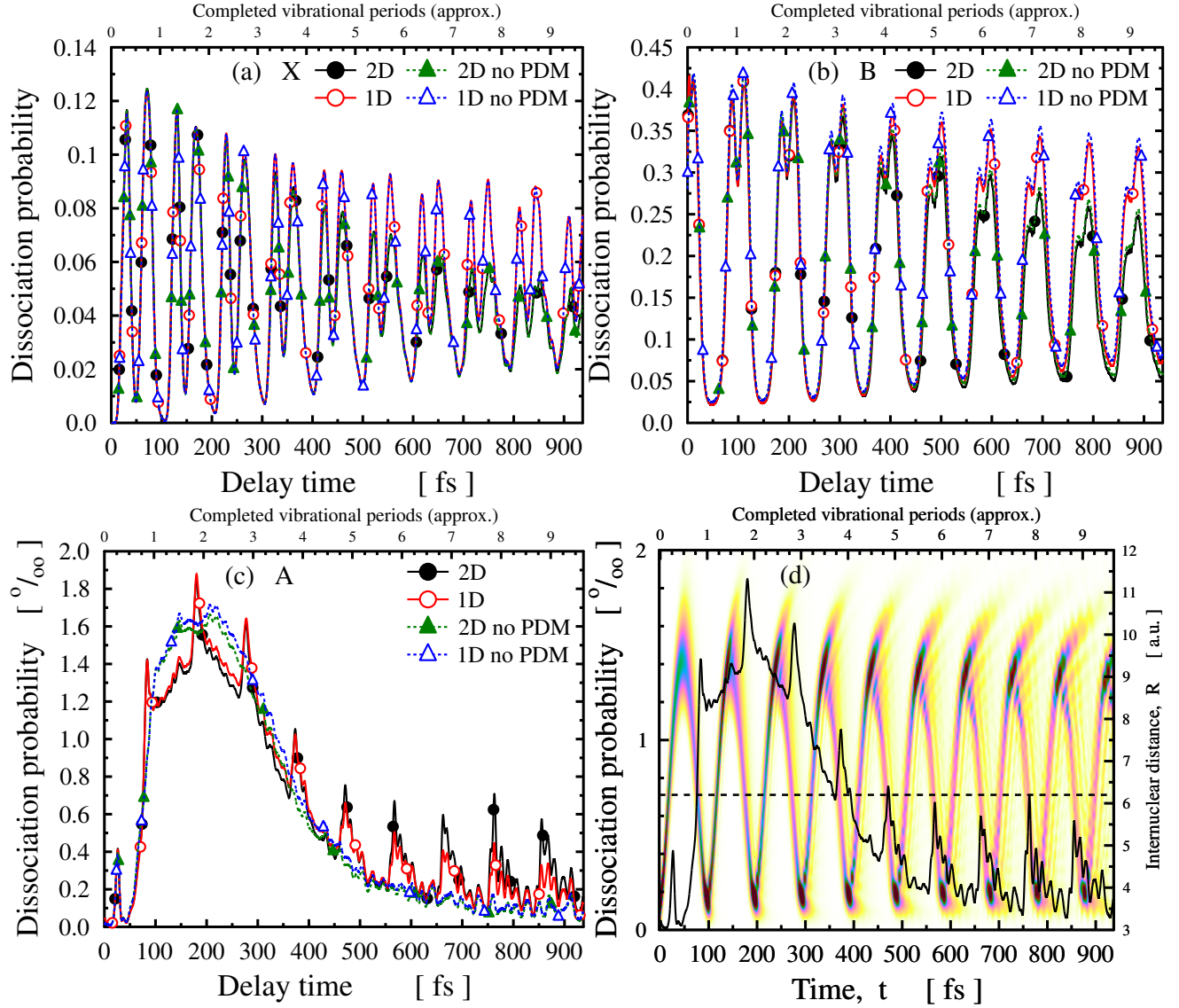


Figure 9: Dissociation probabilities corresponding to each of the individual states as a function of time delay between the pump and probe pulses. Calculations are displayed both of the 1D and 2D schemes neglecting the permanent dipole moments (on panels (a), (b) and (c)) as well. Shown are the results (panel (d)) for 2D dissociation probability of the $V_A(R)$ state with PDM (scaled in left side) and the field-free vibrational motion of the nuclear wave packet (scaled in right-side).

role of the permanent dipole moment of the $V_A(R)$ state. The curve of the dissociation yield of state $V_A(R)$ is significantly modified by the effect of the PDM. Its shape possesses a fairly rich structure and shows some regular spike-like peaks compared to the simple behavior of the dissociation probability calculated without applying the PDM. Additional numerical simulations have shown that the background curve on the dissociation probability of surface $V_A(R)$ is clearly due to that some amounts of the population are transferred back to surface $V_A(R)$ by the probe pulse from the dissociation region of surface $V_B(R)$. The rising of this curve, during the period of (50-150) fs, coincides with that period when the wave packet on the $V_B(R)$ state arrives to the dissociative region (\sim at 12 au). While the decrease, starting at \sim 250 fs, is the result of an artificial effect, caused by the absorption of the wave packet in the CAP region at the end of the grid. Further analyzing the result, one can notice that the peaks appear when the wave packet comes back from the right side of $V_A(R)$, and gets close to the minima of the potential energy surface. (see Fig. 9d). In order to understand better the dissociation process happening on the $V_A(R)$ surface, several different simulations have been performed using model PDM and TDM functions. At first, we set the value of the PDM as $\mu_A = 2.5$ au. The peaks do not appear in this case either, and the obtained result is almost entirely identical to the curve calculated with $\mu_A = 0$ au. The position of the peaks, except for only one case (the first spike), is determined by the delay times when the distance of the atoms approaching each other coincides with the minimum of the $V_A(R)$ potential curve (see Fig. 9d). The size of the spikes, on the other hand, is greatly influenced by the slope of the μ_A function. If the permanent dipole function is steeper, the peaks of the spikes are higher, but if the function is less steep, the peaks of the spikes are lower. In the limiting case, if the dipole function approaches to a constant value, the spikes disappear.

In summary, the resulting dissociation probability of the $V_A(R)$ state is a complex effect of many factors. It is influenced by the minimum of $V_A(R)$ and its coupling to the other two states, as well as the shape of the μ_A dipole moment function etc., but from our current study it is not clear yet what the main underlying processes are.

In Fig. 10 the fragment angular distribution is displayed of the $V_A(R)$ state in 2D with and without using PDM. Although, as it has already been revealed that the dissociation product of the

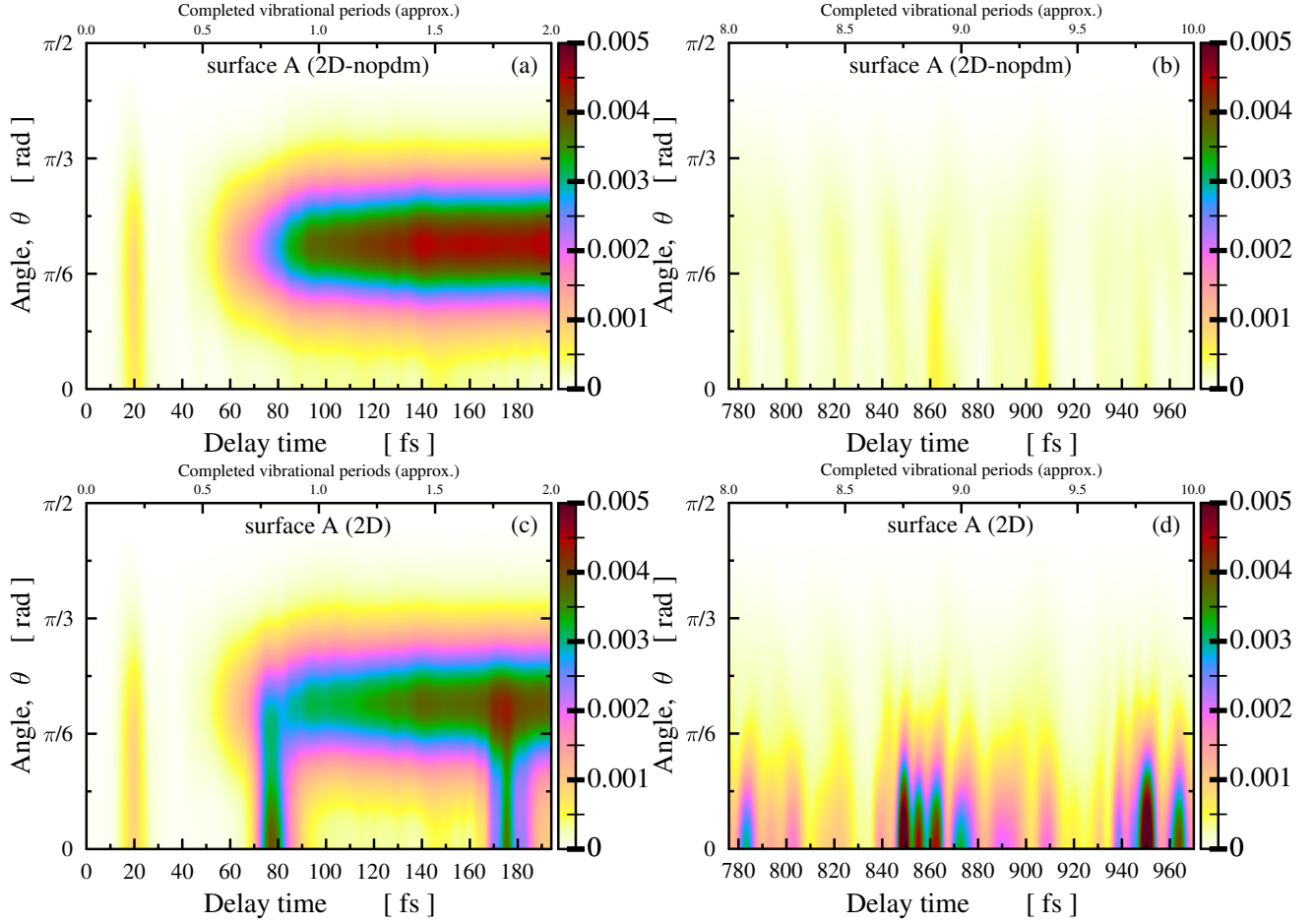


Figure 10: Fragment angular distribution of the dissociating NaH molecule for the $V_A(R)$ electronic state as a function of time delay. Results are presented for the 2D model both the cases of neglecting and including the permanent dipole moment.

$V_A(R)$ state is two orders of magnitude smaller than that of the $V_X(R)$ and $V_B(R)$ states, it is attention-grabbing that the PDM significantly influences the result. It can be observed that the dissociation yield significantly increases in the vicinity of $\theta = 0$ degree which can be seen as the direct consequence of the joint effect of the rotation as well as the LIC1 and LIAC between the $V_A(R)$ and the two other states. The rotation becomes even more efficient due to the effect of the PDM and because considerable two-photon effect can be caused by the probe pulse, larger amount of population could transfer back with sufficient kinetic energy from the $V_X(R)$ and $V_B(R)$ states to the $V_A(R)$ one, so as to enhance the dissociation. The spikes that appear at around $\theta = 0$ degree at small delay times are also due to the PDM and these become stronger at larger delay times due to the increased kinetic energy gathered from the rotation.

IV. Conclusions

In summary, we have discussed the impact of the light-induced non-adiabatic effect as well as the molecular rotation on the dissociation dynamics of the NaH molecule. The three lowest lying electronic states were involved in the pump and probe numerical calculations. Obtained results clearly demonstrated that the permanent dipole moments of the molecule do not play a considerable role in the total dissociation yield, at least for the laser parameters applied. The latter, essentially arrives from the dissociation yields of $V_X(R)$ and $V_B(R)$ states for which the effect of PDM is practically negligible.

However, the inclusion of the permanent dipole moment of the $V_A(R)$ state resulted in a rich pattern on the curve of the dissociation yield. The shape of the curve itself originates from the back-transferred population to the $V_A(R)$ state initiated by the probe pulse from the dissociation region of surface $V_B(R)$. The regular peaks displayed are due to the permanent dipole moment of surface $V_A(R)$ and their height is strongly affected by the gradient of the μ_A function, apart from the initial peak. An additional spectacular trace of these peaks appear too, in the fragment angular distribution. Nevertheless, the underlying physical mechanism, behind of the formation of these peaks, is not yet clear. For the in-depth further understanding and explaining of our current

findings, more detailed analysis is required.

In the future, we plan to perform further investigations for this system. This will include new studies using larger energies for the probe pulse so as to create new LICIs between the $V_X(R)$ and $V_B(R)$ states, as well as applying different pump and probe intensities to discuss properly the one and two photon processes. To understand precisely the behavior of the dissociation of the $V_A(R)$ state further analyses are needed which can be the subject of the forthcoming studies.

Acknowledgment

The authors are indebted to NKFIH for funding (Grant No. K146096). A.C. is grateful for the support of the János Bolyai Research Scholarship (BO/00474/22/11) of the Hungarian Academy of Sciences. This work was supported by the ÚNKP-23-5 New National Excellence Program of the Ministry for Culture and Innovation from the source of the National Research, Development and Innovation Fund.

References

- [1] A. D. Bandrauk and O. Atabek, *J. Phys. Chem.*, 1987, 91, 6469-.
- [2] E. E. Aubanel and A. D. Bandrauk, *J. Chem. Phys.*, 1993, 97, 12620-.
- [3] Y. Arasaki, S. Scheit and K. Takatsuka, *J. Chem. Phys.*, 2013, 138, 161103.
- [4] S. Scheit, Y. Arasaki and K. Takatsuka, *J. Chem. Phys.*, 2014, 140, 244115.
- [5] A.K. Tiwari, D. Dey and N.E. Henriksen, *Phys. Rev. A*, 2014, 89, 023417.
- [6] F. Bouakline, *Chem. Phys.*, 2014, 442, 31-40.
- [7] Y. Arasaki, Y. Mizuno, S. Scheit and K. Takatsuka, *J. Chem. Phys.*, 2016, 144, 024106.
- [8] A. K. Tiwari and N.E. Henriksen, *J. Chem. Phys.*, 2016, 144, 014306.
- [9] A. Tóth, P. Badankó, G. J. Halász, Á. Vibók and A. Csehi, *Chem. Phys.*, 2018, 515, 418-426.

- [10] S. Zhaopeng, W. Chunyang, Z. Wenkai and Y. Chuanlu, *J. Chem. Phys.*, 2018, 149, 224307.
- [11] F. Bouakline, *J. Phys. Chem. Lett.*, 2018, 9, 2271–2277.
- [12] A. Tóth, A. Csehi, G. J. Halász and Á. Vibók, *Phys. Rev. A*, 2019, 99, 043424.
- [13] A. Tóth, A. Csehi, G. J. Halász and Á. Vibók, *Phys. Rev. Res.*, 2020, 2, 013338.
- [14] S. Zhaopeng and L. Yunquan, *Phys. Chem. Chem. Phys.*, 2023, 25, 17397-17402.
- [15] Y. R. Liu, V. Kimberg, Y. Wu, J. G. Wang, O. Vendrell and S. B. Zhang, *Phys. Rev. Res.*, 2022, 4, 043001.
- [16] X. X. Dong, M. Gong, X. Zhao, Y. R. Liu, Y. Cheng, Y. Wu, J. Wang, J. Chen and S. B. Zhang, *New. J. Phys.*, 2024, 10.1088/1367-2630/ad1e92.
- [17] I. R. Solá, J. González-Vázquez, R. de Nalda and Bañares, *Phys. Chem. Chem. Phys.*, 2015, 17, 13183.
- [18] A. Bouallagui, A. Zanchet, L. Bañares, A. García-Vela, *Phys. Chem. Chem. Phys.*, 2023, 25, 20365-20372.
- [19] P. Recio, J. Cachón, A. Zanchet, S. M. Poullain and L. Bañares, *J. Chem. Phys.*, 2023, 158, 234304.
- [20] J. Cachón, P. Recio, A. Zanchet, S. M. Poullain and L. Bañares, *J. Chem. Phys.*, 2023, 159, 064302.
- [21] M. Saab, L. J. Doriol, B. Lasorne, S. Guérin and F. Gatti, *Chem. Phys.*, 2014, 442, 93-102.
- [22] M. Saab, M. Sala, B. Lasorne, F. Gatti and S. Guérin, *J. Chem. Phys.*, 2014, 141, 134114.
- [23] F. Gatti, *Nature* 2018, 557, 641-642.
- [24] C. Sanz-Sanz, G. W. Richings and G. A. Worth, *Faraday Discussions*, 2011, 153, 275-.
- [25] G. A. Worth and G. W. Richings, *Annu. Rep. Prog. Chem., Sect. C: Phys. Chem.*, 2013, 109, 113-.

- [26] C. Robertson and G. A. Worth, *Phys. Chem. Chem. Phys.*, 2017, 19, 29483-29497.
- [27] J. Gonzalez-Vazquez, I. R. Sola, J. Santamaria and V. S. Malinovsky, *Chem. Phys. Lett.*, 2006, 431, 231.
- [28] H. Choi, W. J. Son, S. Shin, B. Y. Chang and I. R. Sola, *J. Chem. Phys.*, 2008, 128, 104315.
- [29] B. Y. Chang, H. Choi, S. Shin, S. Lee and I. R. Sola, *J. Mod. Opt.*, 2009, 56, 811.
- [30] S. Carrasco, J. Rogan, J. A. Valdivia, B. Y. Chang, V.S. Malinovsky, I.R. Sola, *Phys. Chem. Chem. Phys.*, 2022, 24, 2966-2973.
- [31] S. Carrasco, J. Rogan, J.A. Valdivia, I.R. Sola, *Phys. Chem. Chem. Phys.*, 2022, 23, 1936-1942.
- [32] V. Tagliamonti, P. Sándor, A. Zhao, T. Rozgonyi, P. Marquetand and T. Weinacht, *Phys. Rev. A*, 2016, 93, 051401.
- [33] W. O. Rasmus, K. Acheson, P. Bucksbaum, M. Centurion, E. Champenois, et al., *Phys. Chem. Chem. Phys.*, 2022, 24, 15416-15427.
- [34] V. Singh, C. Cheng, T. Weinacht and S. Matsika, *Phys. Chem. Chem. Phys.*, 2022, 24, 20701-20708.
- [35] A.-A. Farcaş and A. Bende, *Phys. Chem. Chem. Phys.*, 2021, 23, 4784-4795.
- [36] A. Bende and A.-A. Farcaş, *Int. J. Mol. Sci.*, 2023, 24, 2906-
- [37] M. Born and R. Oppenheimer, *Ann. Phys.*, 1927, 84, 457-484.
- [38] H. Köppel, W. Domcke and L. S. Cederbaum, *Adv. Chem. Phys.*, 1984, 57, 59-246.
- [39] D. R. Yarkony, *Rev. Mod. Phys.*, 1996, 68, 985-1013.
- [40] G. A. Worth and L. S. Cederbaum, *Annu. Rev. Phys. Chem.*, 2004, 55, 127-158.
- [41] W. Domcke, D. R. Yarkony and H. Köppel, *Conical Intersections: Electronic Structure, Dynamics and Spectroscopy*; World Scientific: Singapore; 2004.

- [42] M. Baer, Beyond Born Oppenheimer: Electronic Non-Adiabatic Coupling Terms and Conical Intersections, Wiley: Hoboken, NJ, 2006.
- [43] N. Moiseyev, M. Sindelka and L. S. Cederbaum, *J. Phys. B*, 2008, 41, 221001.
- [44] G. J. Halász, M. Sindelka, N. Moiseyev, L. S. Cederbaum and Á. Vibók, *J. Phys. Chem. A*, 2012, 116, 2636-.
- [45] G. J. Halász, Á. Vibók, N. Moiseyev and L. S. Cederbaum, *Phys. Rev. A*, 2013, 88, 043413.
- [46] G. J. Halász, A. Csehi, Á. Vibók and L.S. Cederbaum, *J. Phys. Chem. A*, 2014, 118, 11908.
- [47] G. J. Halász, Á. Vibók and L. S. Cederbaum, *J. Phys. Chem. Lett.*, 2015, 6, 348-.
- [48] A. Csehi, G. J. Halász, L. S. Cederbaum and Á. Vibók, *J. Chem. Phys.*, 2015, 143, 0143305.
- [49] A. Csehi, G. J. Halász, L. S. Cederbaum and Á. Vibók, *J. Chem. Phys.*, 2016, 144, 8-.
- [50] A. Csehi, G. J. Halász, L. S. Cederbaum and Á. Vibók, *Faraday Discuss.*, 2016, 194, 479-.
- [51] A. Csehi, G. J. Halász, L. S. Cederbaum and Á. Vibók, *J. Phys. Chem. Lett.*, 2017, 8, 1624-.
- [52] T. Szidarovszky, G. J. Halász, A. G. Császár, L. S. Cederbaum and Á. Vibók, *J. Phys. Chem. Lett.*, 2018, 9, 2239-.
- [53] C. C. Shu, K. J. Yuan, D. Dong, I. R. Petersen and A. D. Bandrauk, *J. Phys. Chem. Lett.*, 2017, 8, 1-.
- [54] A. Natan, M. R. Ware, V. S. Prabhudesai, U. Lev, B. D. Bruner, O. Heber and P. H. Bucksbaum, *Phys. Rev. Lett.*, 2016, 116, 143004.
- [55] M. Kübel, M. Spanner, Z. Dube, A. Yu. Naumov, S. Chelkowski, A. D. Bandrauk, M. J. J. Vrakking, P. B. Corkum, D. M. Villeneuve & A. Staudte, *Nat. Com.*, 2020, 11, 2596-.
- [56] J. Kim, H. Tao, J. L. White, V. S. Petrović, T. J. Martinez and P. H. Bucksbaum, *J. Phys. Chem. A*, 2012, 116, 2758-.

- [57] M. E. Corrales, J. González-Vázquez, G. Balerdi, I. R. Solá, R. de Nalda and L. Bañares, *Nature Chem.*, 2014, 6, 785-.
- [58] C. Fábri, B. Lasorne, G. J. Halász, L. S. Cederbaum and Á. Vibók, *J. Phys. Chem. Lett.*, 2020, 11, 5324-.
- [59] A. Bhattacharjee and K. R. Dastidar, *Phys. Rev. A*, 2002, 65, 022701.
- [60] M. Aymar, J. Deiglmayr and O. Dulieu, *Can. J. Phys.*, 2009, 87, 543-.
- [61] A. Bhattacharjee and K. R. Dastidar, *J. Phys. B: At. Mol. Opt. Phys.*, 2003, 36, 4467-.
- [62] Q. Guo, J.-W. Hu, J. Qi, J. Yu and Y.-C. Han, *Laser Physics*, 2022, 32, 045701.
- [63] H. J. Werner, P. J. Knowles, G. Knizia, F. R. Manby, M. Schütz, et al. MOLPRO, version 2015.1, a package of ab initio programs. 2015; see <http://www.molpro.net> (accessed May 11, 2016).
- [64] E. S. Sachs, J. Hinze and N. H. Sabelli, *J. Chem. Phys.*, 1975, 62, 3367–3376.
- [65] E. S. Sachs, J. Hinze and N. H. Sabelli, *J. Chem. Phys.*, 1975, 62, 3384–3388.
- [66] H. D. Meyer, U. Manthe and L. S. Cederbaum, *Chem. Phys. Lett.*, 1999, 165, 73-.
- [67] G. A. Worth, et. al. The MCTDH package, version 8.6, University of Heidelberg, Germany; <http://mctdh.uni-hd.de/> 2023.
- [68] H. D. Meyer, F. Gatti and G. A. Worth, *Multidimensional Quantum Dynamics: MCTDH Theory and Applications* (Weinheim: Wiley-VCH) 2009.